

# Light-induced chiral gauge field in a massive 3D Dirac electron system

## Authors:

Naotaka Yoshikawa<sup>1\*</sup>, Yoshua Hirai<sup>1</sup>, Kazuma Ogawa<sup>1</sup>, Shun Okumura<sup>2</sup>, Kohei Fujiwara<sup>3</sup>, Junya Ikeda<sup>3</sup>, Takashi Koretsune<sup>4</sup>, Ryotaro Arita<sup>5,6</sup>, Aditi Mitra<sup>7</sup>, Atsushi Tsukazaki<sup>3,8</sup>, Takashi Oka<sup>2</sup>, Ryo Shimano<sup>1,9\*</sup>

## Affiliations:

<sup>1</sup> Department of Physics, The University of Tokyo, Hongo, Tokyo 113-0033, Japan.

<sup>2</sup> Institute for Solid State Physics, The University of Tokyo, Kashiwa 277-8581, Japan

<sup>3</sup> Institute for Materials Research, Tohoku University, Sendai 980-8577, Japan.

<sup>4</sup> Department of Physics, Tohoku University, Miyagi 980-8578, Japan

<sup>5</sup> RIKEN Center for Emergent Matter Science, 2-1 Hirosawa, Wako 351-0198, Japan

<sup>6</sup> Research Center for Advanced Science and Technology, University of Tokyo, Meguro, Tokyo 153-8904, Japan

<sup>7</sup> Center for Quantum Phenomena, Department of Physics, New York University, 726 Broadway, New York, NY, 10003, USA

<sup>8</sup> Center for Science and Innovation in Spintronics (CSIS), Core Research Cluster, Tohoku University, Sendai 980-8577, Japan.

<sup>9</sup> Cryogenic Research Center, The University of Tokyo, Yayoi, Tokyo 113-0032, Japan.

\*Correspondence to: yoshikawa@thz.phys.s.u-tokyo.ac.jp, shimano@phys.s.u-tokyo.ac.jp

## Abstract

The concept of the chiral gauge field (*CGF*), originally developed in theoretical particle physics, has now emerged in condensed matter systems in materials known as Weyl semimetals. In general, Weyl semimetals emerge from Dirac semimetals when time-reversal or spatial-inversion symmetries are broken. Recently, it has gained a growing interest to manipulate such topological states of matter by implementing the *CGF* by shining light to materials. Here we have demonstrated the emergence of *CGF* in a massive 3D Dirac electron system in the paramagnetic phase of  $\text{Co}_3\text{Sn}_2\text{S}_2$ , which exhibits a ferromagnetic Weyl semimetal phase at low temperatures. We first show theoretically that the illumination of circularly polarized light implements the *CGF* in the paramagnetic state of  $\text{Co}_3\text{Sn}_2\text{S}_2$  and gives rise to a topological Weyl state, which can be realized only in the nonequilibrium state. Then we demonstrated that the presence of light-induced *CGF* through the observation of light-induced anomalous Hall effect, the behavior of which quantitatively agrees with the calculation from the Floquet theory. The light-induced AHE manifests the Berry curvature which becomes nonzero as the bands split due to the light-induced *CGF*. Our demonstration paves a new pathway for ultrafast manipulation of topological phases in 3D Dirac semimetals and for further exploring new quantum matter phases which can be only achieved by light.

## Main text

### I. INTRODUCTION

Three-dimensional (3D) Dirac semimetals (DSMs) and Weyl semimetals (WSMs) have gained a growing interest because of the presence of massless quasiparticles around the linearly crossing electronic bands, that effectively act as Dirac and Weyl fermions, respectively [1–7]. These quantum materials exhibit various intriguing physical properties such as large linear magnetoresistance [8], chiral-anomaly-induced negative magnetoresistance [9,10], surface Fermi arc states [11], unusual quantum oscillations [12], and intrinsic anomalous Hall effect (AHE) [13]. Such electronic and optical functionalities mostly associated with the topological properties have made DSMs and WSMs highly attractive from fundamental and practical points of view.

Light is considered an ideal tool for manipulating quantum electronic states of matter in an ultrafast manner. Ultrafast dynamics of electrons in DSMs and WSMs have been intensely investigated recently, revealing novel optoelectronic phenomena such as the circular photogalvanic and photovoltaic effects [14–17], which are related to the coupling between the light polarization and the pseudospin of the massless fermions. Furthermore, transient modifications of the crystal symmetry characterizing the inversion-symmetry

breaking WSM states by light have been reported as a route to the dynamically induced topological phase transition via the phonon excitation or photocurrent generation [18–20].

Distinct from these processes accompanying the optical excitation of quasiparticles or collective modes, Floquet engineering has been proposed as a unique pathway to directly control the topological invariant by coherent driving by light [21–23]. Strikingly, it has been predicted that a time-periodic field of circularly polarized light (CPL) in 3D DSMs acts as chiral gauge field (CGF), which couples oppositely to the left- and right-handed fermions [24–28]. This time-reversal symmetry (TRS) breaking perturbation leads to the emergence of Floquet-WSM states by splitting a DP into a pair of WPs. In the case of massless (gapless) 3D DSMs, the separation of the Floquet-WPs in momentum space corresponds to twice of the CGF  $\mathbf{A}_5 = \beta \hat{\mathbf{z}}$  perpendicular to the polarization plane of irradiated CPL with its magnitude scaling as  $\beta \propto E^2/\Omega^3$  ( $E$ : electric field strength,  $\Omega$ : angular frequency of the driving field) [25,27]. The pair of WPs behaves as a source and sink of Berry curvature [1–7], which characterizes the nontrivial band topology of the Floquet-Weyl state. Since the CGF is also responsible for topological electromagnetic responses in WSMs such as AHE and chiral magnetic effect, the experimental realization of light-induced CGF is anticipated for the manipulation of those emergent topological phenomena. The implement of CGF can be tuned by the direction and intensity of light, leading to versatile topological phases which only appear in the nonequilibrium state [26–28].

In general, 3D Dirac nodes are unstable because the degeneracy at Dirac points (DPs) is not topologically protected unlike the case of Weyl nodes. The existence of gapless DPs often requires the fine-tuning of material parameters for accidental degeneracy [29–33], while in some materials this degeneracy is enforced by symmetry [11,34–37]. Even in the latter case, the Dirac nodes can be gapped out by small symmetry-breaking perturbations such as lattice deformation [38]. However, robust Floquet-WPs can appear even in massive (gapped) 3D DSMs when the induced CGF is large enough to close the mass gap [25,27]. This highlights another intriguing aspect of the Floquet-WSM state, namely, one can create topologically protected massless fermions in DSMs with a mass gap due to the lack of accidental or symmetry-enforced degeneracy. Experimentally, Floquet topological insulator state, which emerges in CPL-driven two-dimensional honeycomb lattice systems, has been demonstrated in synthesized systems [39,40] and also proposed in graphene [41]. However, in contrast to intensive theoretical studies, the experimental demonstration of Floquet-Weyl state remains unresolved.

## II. EXPERIMENT

In order to investigate the Floquet-WSM states emergent in a 3D Dirac semimetal, we focus on the Kagome-lattice shandite  $\text{Co}_3\text{Sn}_2\text{S}_2$  (Fig. 1(a)).  $\text{Co}_3\text{Sn}_2\text{S}_2$  has recently attracted considerable attention due to the emergence of the ferromagnetic WSM phase below the Curie temperature  $T_C$  around 180 K [42,43], while it also provides a playground for investigating 3D Dirac electron system in its paramagnetic phase above  $T_C$ . In its ferromagnetic phase,  $\text{Co}_3\text{Sn}_2\text{S}_2$  shows three pairs of Weyl nodes with linearly dispersing bands in the 3D momentum space, which arises from band inversion, exchange splitting, and spin-orbit coupling (SOC). Without SOC, the valence and conduction bands invert near the  $L$  points of the Brillouin zone, which forms nodal rings protected by the mirror symmetry. The spin band degeneracy is lifted by the exchange coupling in the ferromagnetic phase. The nodal rings are gapped out by including SOC associated with the out-of-plane spin, except for three pairs of linearly crossing points which give rise to Weyl nodes [42–44].

In the paramagnetic phase above  $T_C$ , another type of SOC associated with the in-plane spin is considered to cause additional level repulsions between the electronic states at the linearly crossing DPs. First-principles calculations reveal that the original nodal rings are fully gapped out by including SOC in the paramagnetic state (for the band calculations see Appendix A) [45,46]. The energy separation of the two bands has a minimum value of about 10 meV, around which the electronic band structure can be regarded as that of a massive 3D DSM.

As a sample, we used a 23 nm-thick  $\text{Co}_3\text{Sn}_2\text{S}_2$  film grown on a sapphire substrate [47] (See Appendix B for details). All the measurements were performed at room temperature, which is far above the ferromagnetic transition temperature of  $T_C=185$  K. A mid-infrared (MIR) femtosecond pulse was used as a periodic driving field to implement a sufficient CGF ( $\propto E^2/\Omega^3$ ) without inducing material damage. The photon energy of 0.31 eV ( $\Omega/2\pi = 75$  THz) was selected to be larger than the energy scale of the linearly dispersing bands in  $\text{Co}_3\text{Sn}_2\text{S}_2$  [48,49]. In this way we avoided the effect of Berry curvature associated with the band crossing point of the Floquet replica (photon-dressed) states [26] and made the Berry curvature distribution at around the original DPs dominate the light-induced AHE, which verifies the interpretation based on the Floquet theory with high-frequency expansion.

### III. RESULT

#### 1. Effective model for the Floquet state of $\text{Co}_3\text{Sn}_2\text{S}_2$

Before going into experimental results, we first introduce an effective model developed to describe the Floquet band structure of  $\text{Co}_3\text{Sn}_2\text{S}_2$ . We start with the gapless 3D Dirac

system, and then extend to the gapped one. The electronic state with pairs of 3D Dirac nodes can be modeled by,

$$H_{\text{eq}}(\mathbf{k}) = H_{\text{NR}}(\mathbf{k}) + H_{\text{SO},z}(\mathbf{k}),$$

$$H_{\text{NR}}(\mathbf{k}) = [M - Bk^2]\tau_z s_0 + vk_x \tau_x s_0, \quad (1)$$

$$H_{\text{SO},z}(\mathbf{k}) = \Delta_{\text{SO}} k_y \tau_y s_z,$$

where  $H_{\text{NR}}(\mathbf{k})$  describes a nodal-ring semimetal and properly chosen SOC,  $H_{\text{SO},z}(\mathbf{k})$ , gaps it out leaving two Dirac nodes in momentum space (Fig. 1(b)). Here, we assume  $\hbar = e = 1$ .  $M$  and  $B$  are positive constants,  $v$  refers to the Fermi velocity along the  $x$ -direction, and  $\Delta_{\text{SO}}$  quantifies the out-of-plane type of SOC.  $\tau_{x,y,z}$  ( $s_{x,y,z}$ ) and  $\tau_0$  ( $s_0$ ) are Pauli matrices and the identity matrix for the orbital (spin) quantum number, respectively. The energy bands projected to  $k_x = k_y = 0$  around the DP are also plotted in the inset of Fig. 1(b). Then, the time-independent effective Hamiltonian with right-hand CPL along the  $z$ -direction  $(\frac{E}{\Omega} \cos(\Omega t), -\frac{E}{\Omega} \sin(\Omega t), 0)$  is given by applying Peierls substitution and high-frequency expansion [21,23,28,50];

$$\begin{aligned} H_{\text{eff}}(\mathbf{k}) \approx & [(\tilde{M} - Bk^2)s_0 - \beta s_z]\tau_z + \left(v s_0 + \frac{2\beta B s_z}{v}\right)k_x \tau_x \\ & + \left(\frac{2\beta B s_0}{\Delta_{\text{SO}}} + \Delta_{\text{SO}} s_z\right)k_y \tau_y, \\ \tilde{M} = & M - \frac{E^2 B}{\Omega^2}, \\ \beta = & \frac{E^2 v \Delta_{\text{SO}}}{\Omega^3}. \end{aligned} \quad (2)$$

By diagonalizing this  $4 \times 4$  effective Hamiltonian, the Floquet band structure is obtained as drawn in Fig. 1(c). The linear band crossing appears at  $K_{\pm,\delta} = (0, 0, \pm\sqrt{(\tilde{M} - \delta\beta)/B})$  in the spin up ( $\delta = +1$ ) and down ( $\delta = -1$ ) bands, which corresponds to the emergence of Floquet-WSM state where each DP splits into a pair of WPs. The emergent four WPs are also indicated with their chirality as  $\text{WP}_+$  and  $\text{WP}_-$  in the projected energy bands in the inset of Fig. 1(c). The Berry curvature distribution in the  $k_y = 0$  plane of the Floquet-WSM state is also displayed, which gives rise to the AHE.

Next, to describe the massive 3D DSM state in  $\text{Co}_3\text{Sn}_2\text{S}_2$ , another in-plane type of SOC,  $H_{\text{SO},x} = m\tau_y s_x$ , is added to  $H_{\text{eq}}$  which gaps out the DPs with the gap energy of  $2m$

(Fig. 1(d)). Considering this term as  $k$ -independent, the effective Hamiltonian under CPL irradiation is obtained by simply adding  $H_{\text{SO},x}$  to eq. (2). The calculated Floquet band structure is represented in Fig. 1(e) and 1(f) for two regimes of the field strength. When the induced CGF is smaller than the equilibrium gap energy ( $\beta < m$ ), the degenerated spin bands are lifted by breaking the TRS. As  $\beta$  increases, the original gap closes at  $\beta = m$  and the pairs of WPs appear under  $\beta > m$ .

The WPs configuration and the Berry curvature distribution for  $\beta > m$  are essentially the same as that for the Floquet-WSM state arising in the massless 3D DSM state shown in Fig. 1(c). The induced anomalous Hall conductivity (AHC) of the Floquet state of  $\text{Co}_3\text{Sn}_2\text{S}_2$  was calculated from linear response theory [51,52] (for details see Appendix C). For this calculation we also take into account the propagation direction of the CPL tilting from the separation of the DPs. Importantly, a finite AHC is observed even for  $\beta < m$  because of the nonzero value of the integrated Berry curvature over the occupied bands which are split by the induced CGF. Note also that the present Floquet-WSM state has a distinct energy band and Berry curvature distribution from the equilibrium ferromagnetic WSM phase of  $\text{Co}_3\text{Sn}_2\text{S}_2$  below  $T_C$  (Appendix D). This manifests a practical example of topological phases realized by Floquet engineering, which can be achieved only in the nonequilibrium state.

## 2. Light-induced anomalous Hall effect in $\text{Co}_3\text{Sn}_2\text{S}_2$

To demonstrate the AHE in the CPL-driven Floquet state, we performed MIR pump-terahertz (THz) Faraday probe spectroscopy as illustrated in Fig. 2(a) (for details see Appendix E). The circularly polarized MIR pump pulse induced the CGF on the Dirac electrons, and the resulting AHE was detected by measuring the Faraday rotation of the probe THz pulse, where the low photon energy ( $\sim 0.01$  eV) THz pulse was used as an ultrafast probe of the Hall conductivity. Figure 2(b) presents time evolutions of the THz Faraday rotation of the  $\text{Co}_3\text{Sn}_2\text{S}_2$  film induced by the MIR pump pulse with the peak electric field  $E = 1.1 \text{ MV cm}^{-1}$  inside the film, for left-hand circular polarization ( $\sigma^-$ , blue open circles) and right-hand circular polarization ( $\sigma^+$ , red open circles). Grey line in Fig. 2(b) indicates the cross-correlation waveform between the pump MIR pulse and the near-infrared pulse used for the optical sampling of the probe THz pulse, which defines the response function of our pump-probe setup. The temporal profile of the observed Faraday rotation signal overlaps this cross-correlation waveform, indicating that the signal arises from a pump pulse-driven coherent transient effect.

The complex Faraday rotation angle,  $\Theta(\omega) = \theta(\omega) + i\eta(\omega)$  is directly linked to the Hall conductivity  $\sigma_{xy}$  in the frequency domain by the equation  $\Theta(\omega) \cong \sigma_{xy}(\omega)d/$

$[(1 + n_{\text{sub}})c\epsilon_0 + \sigma_{xx}(\omega)d]$  for the thin-film sample, where  $n_{\text{sub}}$  is the refractive index of the substrate,  $c$  is the speed of light,  $\epsilon_0$  is the vacuum permittivity,  $\sigma_{xx}(\omega)$  represents the longitudinal optical conductivity, and  $d$  is the thickness of the film sample. Figure 2(c) and 2(d) show the spectra of the CPL-induced Faraday rotation  $\Delta\theta$  and ellipticity  $\Delta\eta$  measured at  $t_{\text{pp}} = 0$ . The AHC  $\Delta\sigma_{xy}(\omega)$  is then obtained by using the above equation as plotted in Fig. 2(e) and 2(f).

### 3. Fluence and frequency dependence

To have a deeper insight into the CPL-induced AHE, we examined the fluence and frequency dependence of the AHC spectrum  $\Delta\sigma_{xy}(\omega)$ . Figure 3(a) and 3(b) present the fluence dependence of the real- and imaginary part of the THz AHC spectra, respectively, induced by the CPL (at  $t_{\text{pp}} = 0$  in Fig. 2(b)). The magnitude of the real-part AHC ( $\text{Re}[\Delta\sigma_{xy}]$ ) monotonically increases on increasing the fluence. The imaginary part of the Hall conductivity ( $\text{Im}[\Delta\sigma_{xy}]$ ) is close to zero and virtually unchanged as the fluence increases. The observed spectral features are well reproduced by the theoretical calculation from the linear response theory (for details see Appendix A).

Figure 3(c) shows the amount of CPL-induced AHC as a function of the excitation fluence for various pump frequencies. Here, we plotted the average values of AHC between 6.2 and 10.3 meV (we chose this range by considering our experimental situation, for details see Appendix F). The result indicates that the magnitude of the AHC depends not only on the pump fluence but also on the pump frequency, where the lower frequency excitation induces AHC more efficiently than the higher frequency excitation. Notably, the AHC at various pump frequencies is scaled into one curve when plotted as a function of  $E^2(\hbar\Omega)^{-3}$  which is proportional to the CGF, and linearly increases in the weak excitation regime (Fig. 3(d)). Red line in Fig. 3(d) indicates the theoretical expectation of the AHC for the case of the Floquet state by assuming the effective model as presented in Fig. 1(d)-1(f). Here, the AHC is calculated by taking into account the finite chemical potential (0.12 eV below the center of the mass gap) and temperature (300 K) relevant to the experiments, which indeed shows the universal scaling nature of  $\sigma_{xy} \propto E^2/\Omega^3$ . Notably, by summing up the contributions of the three pairs of gapped Dirac points, we obtained the same order of magnitude as that measured experimentally. Given that the smaller value in the experiment can be partly attributed to the spatial non-uniformity of the CPL excitation in our experiment (Appendix F) and finite carrier scatterings which should effectively suppress the pump electric field in the ac driving process (Appendix G), we consider that the calculated result using the Floquet theory provides reasonably good agreement with the experimental results. The saturating behavior of  $\sigma_{xy}$  at the high

pump fluence may be attributed to the increase of the carrier scattering rate and broadening of the energy distribution due to the temperature increase of the electron system.

Figure 3e shows the slope of the CPL-induced AHC,  $\sigma_{xy}/E^2$ , obtained by line fitting of the experimental data in the small  $E$  region as a function of pump frequency. One can see that the lower pump frequency induces the AHC more efficiently. This frequency dependence is consistent with the prediction from the Floquet theory, i.e., the  $\Omega^{-3}$ -power law (red curve) within the error bars. It should be noted here that this behavior is distinct from the pump-induced change of longitudinal optical conductivity,  $\text{Re}[\Delta\sigma_{xx}]/\text{Re}[\sigma_{xx}]$ , which is nearly independent of the pump frequency as shown in Fig. 3(f) and also helicity-independent (details are shown in Appendix H). This frequency-independent nature of  $\Delta\sigma_{xx}$  is rather reasonable because it is attributed to the pump-induced change of carrier density and/or scattering rate of the metallic carriers, and the absorption ratio of the pump photon is nearly identical in the investigated pump frequency range.

#### IV. DISCUSSION

Here we address other possible origins of CPL-induced AHE, namely the inverse Faraday effect (IFE) and the population effect [53,54]. To examine IFE by which the CPL induces the magnetization along the propagation axis, we consider the CPL-induced Zeeman term in the effective model of  $\text{Co}_3\text{Sn}_2\text{S}_2$  via the in-plane SOC (for details see Appendix I). We show that the contribution of the Zeeman term to the AHC is smaller in orders of magnitude than that of the CGF and therefore is excluded as the origin of the observed AHE. The population effect where the asymmetric population of the photocarriers causes the Hall current is also unlikely to explain the AHE in  $\text{Co}_3\text{Sn}_2\text{S}_2$  because (i) the Hall current arising from the photocarrier population does not match the experimentally observed driving frequency dependence by considering that the absorption ratio is almost unchanged in the employed frequency range, and (ii) naively the Hall current by this effect is proportional to the group velocity at the momentum where the population imbalance is generated, and therefore is expected to be small if one considers that the MIR photon corresponds to the optical transition associated with the high energy bands which possess flat dispersion in  $\text{Co}_3\text{Sn}_2\text{S}_2$  [49].

Accordingly, the CPL-induced AHE is most likely attributed to the CGF anticipated to emerge in the 3D Dirac fermion system. Since the initial state is a massive 3D DSM, it depends on the amount of  $\beta$  as to whether the Floquet-WSM is realized or not. The CGF in 3D Dirac system afforded by the CPL propagating the  $z$ -axis is given by  $\beta = (eE)^2 v_{F,x} v_{F,y} / (\hbar\Omega)^3$ , which is estimated to  $\beta = 3.1$  meV for  $\hbar\Omega/2\pi = 75$  THz and



$E = 1.1 \text{ MV cm}^{-1}$  (for the estimation of the Fermi velocities around the DP,  $v_{F,x}$  and  $v_{F,y}$ , see Appendix A). This reaches about 60 % of the amount required for closing the mass gap. Realistic improvements of, e.g., the light source will realize the Floquet-WSM state and allow us to investigate the dynamically emergent topologically protected properties such as chiral anomaly and surface Fermi arc.

## V. CONCLUSION

Importantly, the Floquet-Weyl state investigated in the present work is a unique state appearing only under the illumination of light, and is not achievable in the equilibrium state. The CGF is a prerequisite for the realization of such nonequilibrium topological states of matter, therefore the experimental demonstration of the light-induced CGF ensures that those nonequilibrium topological phases can be indeed achieved within ultrafast time scales. The on-demand topological phase transition by light enables ultrafast switching between the 3D Dirac and Weyl state, and provides a unique pathway for the ultrafast quantum manipulation of topological materials.

## ACKNOWLEDGEMENT

This work was supported by JST CREST grant no. JPMJCR19T3, JPMJCR18T2, Japan. A.M. acknowledges the support by the US Department of Energy, Office of Science, Basic Energy Sciences under Award No. DE-SC0010821.

## APPENDIX A: BAND CALCULATIONS OF THE PARAMAGNETIC PHASE OF $\text{Co}_3\text{Sn}_2\text{S}_2$

We carried out first-principles calculations of the paramagnetic phase of  $\text{Co}_3\text{Sn}_2\text{S}_2$ , based on the noncollinear density functional theory (DFT) using the quantum-ESPRESSO code [55], and analyzed the band structures using the Wannier-interpolated Hamiltonian [56]. The details of the method and results for the ferromagnetic state of  $\text{Co}_3\text{Sn}_2\text{S}_2$  can be found in Ref. [57]. Figure 4(a) and 4(b) represent the calculated band structure of  $\text{Co}_3\text{Sn}_2\text{S}_2$  in the paramagnetic phase, without spin-orbit coupling (SOC) and with SOC, respectively. The band crossing points indicated by blue dotted circles in Fig 4(a) are parts of the nodal ring, which are gapped out by including the SOC. Figure 4(c) and 4(d) display the energy separations of the relevant two bands, without and with the spin-orbit coupling (SOC), respectively. While a nodal ring is formed in  $k_y = 0$  plane in the case of no SOC, the inclusion of the SOC gapped out this nodal ring everywhere. The energy separation has a minimum value of  $\sim 10 \text{ meV}$  at  $(k_x, k_z) = (0.44, 0.03)$  and  $(0.73, 0.37)$ , around which the electronic band structure can be regarded as that of

massive 3D Dirac semimetal (DSM). The band structures including the DP are plotted along  $k_x, k_y, k_z$  directions in Fig. 4(e)-4(g), respectively. From these dispersions, the Fermi velocities around the DP are estimated to be  $\mathbf{v}_F = (v_{F,x}, v_{F,y}, v_{F,z}) = (0.84, 0.85, 1.67) \text{ eV\AA}$ .

## APPENDIX B: SAMPLE PREPARATION AND CHARACTERIZATION

The 23 nm-thick  $c$ -axis-oriented  $\text{Co}_3\text{Sn}_2\text{S}_2$  films were grown on double-side polished  $\text{Al}_2\text{O}_3$  (0001) substrates by radio-frequency magnetron sputtering with a cap of an approximately 50 nm-thick insulating  $\text{SiO}_2$  layer. Detailed information for the fabrication and characterization of the film sample can be found in Ref. [47]. The ferromagnetic transition temperature of the used film samples is identified at  $T_C \sim 185 \text{ K}$ .

## APPENDIX C: CALCULATION OF THE ANOMALOUS HALL CONDUCTIVITY IN THE FLOQUET STATE

Based on the effective model introduced in the main text, we calculated the anomalous Hall conductivity (AHC) spectrum in the Floquet state. Here, the effect of light propagation direction, which is tilted from the separation of the pair of DPs in the experiment as illustrated in Fig. 5(a), is included by applying rotational operation around the  $y$ -axis with a tilted angle  $\phi$ . The modified Hamiltonian for the massless DSM state is written as,

$$\begin{aligned} H_{\text{eq}}(\mathbf{k}) &= [m - Bk'^2]\tau_z s_0 + vk'_x \tau_x s_0 + \Delta_{\text{SO}} k'_y \tau_y s_z \\ &= [m - Bk^2]\tau_z s_0 + v(k_x \cos \phi + k_z \sin \phi) \tau_x s_0 + \Delta_{\text{SO}} k_y \tau_y s_z, \quad (\text{A1}) \end{aligned}$$

$$(k'_x, k'_y, k'_z) = (k_x \cos \phi - k_z \sin \phi, k_y, k_z \cos \phi + k_x \sin \phi).$$

By the same procedure as that for eq. (2), the time-independent effective Hamiltonian under the circularly polarized light (CPL) driving field is given as,

$$H_{\text{eff}}(\mathbf{k}) \approx [(\tilde{M} - Bk^2)s_0 - \beta \cos \phi s_z]\tau_z + v_y k_y \tau_y + (v_x k_x - v_z k_z) \tau_x \quad (\text{A2})$$

$$\text{with } \tilde{M} = m - \frac{BE^2}{\Omega^2}, \beta = \frac{E^2 v \Delta_{\text{SO}}}{\Omega^3}, v_y = \Delta_{\text{SO}} s_z + \frac{2E^2}{\Omega^3} B v \cos \phi s_0, v_x = v \cos \phi s_0 +$$

$\frac{2E^2}{\Omega^3} B \Delta_{\text{SO}} s_z$ , and  $v_z = v \sin \phi s_0$ . Then the two DPs split into the four Weyl points (WPs) at

$$K_{\delta,\pm} = \left( \pm \sqrt{\frac{\tilde{M}_\delta v_{z,\delta}^2}{B(v_{z,\delta}^2 + v_{x,\delta}^2)}}, 0, \pm \sqrt{\frac{\tilde{M}_\delta v_{x,\delta}^2}{B(v_{z,\delta}^2 + v_{x,\delta}^2)}} \right),$$

$$\delta = \pm 1 \text{ and } \tilde{M}_\delta = \tilde{M} - \delta\beta \cos \phi,$$

$$v_{x,\delta} = v \cos \phi + \delta \frac{2E^2}{\Omega^3} B \Delta_{\text{SO}}, \text{ and } v_{z,\delta} = v \sin \phi. \quad (\text{A3})$$

Next, the in-plane type of SOC,  $H_{\text{SO},x} = m\tau_y s_x$ , is added to  $H_{\text{eq}}$  in eq. (A1) to introduce the mass gap. By referring the band structure calculation of  $\text{Co}_3\text{Sn}_2\text{S}_2$ , we adopted a material parameter set,  $M = 0.13 \text{ eV}$ ,  $v = 0.82 \text{ eV \AA}$ ,  $\Delta_{\text{SO}} = 0.85 \text{ eV \AA}$ ,  $B = 1.44 \text{ eV \AA}^2$ ,  $\phi = 40^\circ$ , and  $m = 0.005 \text{ eV}$ . The optical Hall conductivity is calculated from linear response theory [51,52], which leads to

$$\sigma_{\lambda\nu}(\omega) = -\epsilon^{\lambda\nu\rho} \frac{e^2}{\hbar a} \sum_{\alpha \neq \beta} \int \frac{d\mathbf{k}}{(2\pi)^3} \frac{(E_{\alpha\mathbf{k}} - E_{\beta\mathbf{k}})^2}{\omega^2 - (E_{\alpha\mathbf{k}} - E_{\beta\mathbf{k}})^2} f_\alpha(\mathbf{k}) [\nabla_{\mathbf{k}} \times \mathcal{A}_\alpha(\mathbf{k})]_\rho \quad (\text{A4})$$

where  $\lambda, \nu, \rho = x, y, z$ ,  $\epsilon^{\lambda\nu\rho}$  is the Levi-Civita symbol,  $e$  is the elementary charge,  $\hbar$  is the reduced Plank constant,  $a = 5.37 \text{ \AA}$  is the lattice constant, and  $\alpha, \beta$  represent band indices.  $f_\alpha(\mathbf{k}) = (1 + e^{(E_{\alpha\mathbf{k}} - \mu)/T})^{-1}$  is the Fermi distribution function and  $\mathcal{A}_\alpha(\mathbf{k})$  represents the Berry connection. We introduce the angular frequency of the probing light  $\omega$  to compute the ac-response. The temperature  $T$  is set to 300 K and the chemical potential  $\mu$  is set to 0.12 eV below the center of the mass gap. The calculated real and imaginary parts of the  $\sigma_{xy}(\omega)$  spectra are displayed in Fig. 5(b) and 5(c). The calculated spectra show a nearly constant value in the real part and a negligibly small value in the imaginary part, which well matches the experimentally observed spectral feature as shown in Fig. 3(a) and 3(b) in the main text. Since the real part in this energy range can be approximately regarded as a constant, we present the calculated value of  $\sigma_{xy}(\omega/2\pi = 10 \text{ meV})$  in Fig. 3D and 3E in the main text. As one can see in Fig. 5(c) and Fig. 3(d) in the main text, the calculation shows  $\sigma_{xy} \propto \beta \propto E^2/\Omega^3$  even in the weak field regime ( $\beta < m$ ). This is reasonable because an infinitesimal  $\beta$  causes a nonzero value of the integrated Berry curvature over the occupied bands split by the chiral gauge field (CGF), leading to a finite AHE. This result shows that the AHE in  $\text{Co}_3\text{Sn}_2\text{S}_2$  induced by the irradiation of CPL originates from the light-induced CGF even when there still exists a mass gap at the DPs.

#### APPENDIX D: COMPARISON OF THE FLOQUET-WEYL STATE AND THE FERROMAGNETIC WEYL STATE OF $\text{Co}_3\text{Sn}_2\text{S}_2$

As also noted in the main text, the present Floquet-Weyl semimetal state is distinct from the equilibrium ferromagnetic Weyl semimetal state of  $\text{Co}_3\text{Sn}_2\text{S}_2$  which appears below  $T_C$ . In the ferromagnetic phase, the spin-up and -down bands are lifted by the ferromagnetic exchange splitting, forming two sets of WPs at different energies as illustrated in Fig. 6(a) and 6(b). The transport properties are dominated by the spin-majority bands in which WPs lie close to the Fermi energy. The Berry curvature distribution for these spin-majority bands exhibit a source and a sink in the momentum space as shown in Fig. 6(c).

## APPENDIX E: MID-INFRARED PUMP AND THz FARADAY ROTATION MEASUREMENT

The setup for the mid-infrared (MIR) pump-terahertz (THz) Faraday probe measurement is illustrated in Fig. 7. We used a Yb:KGW-based regenerative amplifier (pulse energy 2 mJ, center wavelength 1030 nm, repetition rate 3 kHz, and pulse duration 170 fs) as a light source. Half of the output was used to generate the mid-infrared pump pulse (center wavelength 3.8-4.1  $\mu\text{m}$ , corresponding to 73-79 THz in frequency) by an optical parametric amplifier (OPA). The other half was further split into two beams for the probe THz pulse generation and for the electro-optic sampling of the THz pulse, respectively. The fluence of the mid-infrared pump pulse was tuned by using two ZnSe wire-grid polarizers. The polarization state of the pump pulse was controlled by a liquid-crystal variable retarder. The pump pulse was focused onto the sample using a  $\text{CaF}_2$  lens (focal length: 100 mm) in a normal incident configuration. The duration of the MIR pump pulse was measured by cross-correlation with the fundamental 1030 nm pulse and estimated as 103, 96, 114, and 130 fs for the pump pulse with the center frequency of 73, 75, 77, and 79 THz, respectively.

The probe THz pulse was generated by a 380- $\mu\text{m}$ -thick GaP (110) crystal, and the transmitted THz probe pulse was detected by using an electro-optic sampling method with another 380- $\mu\text{m}$ -thick GaP (110) crystal. The Faraday rotation signal was obtained by measuring the THz electric field with the polarization parallel ( $E_x$ ) and perpendicular ( $E_y$ ) to the incident polarization, by changing the configuration of the wire-grid polarizers (WGP1, WGP2 and WGP3 in Fig. 7). The Faraday rotation angle displayed in Fig. 2(b) plots the obtained value  $\theta = E_y(t)/E_x(t)$  with the sampling pulse fixed at the peak of the probe THz pulse. The complex Faraday rotation angle,  $\Theta(\omega) = \theta(\omega) + i\eta(\omega)$ , where  $\theta(\omega)$  is the Faraday rotation angle  $\eta(\omega)$  is the ellipticity, is determined from the Fourier component of the transmitted probe electric fields as,  $\Theta(\omega) = E_y(\omega)/E_x(\omega)$ . The off-diagonal optical Hall conductivity spectra were then obtained through the relation  $\theta_F(\omega) + i\eta(\omega) \cong \sigma_{xy}(\omega)d/[(1 + n_{\text{sub}})c\epsilon_0 + \sigma_{xx}(\omega)d]$  where  $n_{\text{sub}}$  is the refractive

index of the substrate,  $c$  the speed of light,  $\epsilon_0$  the vacuum permittivity,  $\sigma_{xx}(\omega)$  the longitudinal conductivity, and  $d$  the thickness of the film sample. The delay time between the MIR pump pulse and probe THz pulse with respect to the sampling pulse was controlled by the delay stages (DS1 and DS2). The sample was held in a vacuum, and all the optical measurements were performed at room temperature.

## APPENDIX F: CONSIDERATION OF THE EFFECT OF THE SPATIAL NON-UNIFORMITY OF THE MIR EXCITATION

The spot sizes of the pump MIR pulse and probe THz pulse were evaluated by the knife-edge method. The measured spot size of the MIR pump was  $190\text{ }\mu\text{m}$  in  $1/e$  radius at the sample position. Those for the probe THz pulse were evaluated for each frequency taking into account the difference in diffraction limit within the used spectral range. The obtained values were  $240 \times 310\text{ }\mu\text{m}$  for 1 THz (4.14 meV) and  $140 \times 200\text{ }\mu\text{m}$  for 2 THz (8.27 meV) in  $1/e$  radius. Therefore, the excitation by the MIR pump is not uniform in the whole probed region, which causes the underestimation of the CPL-induced AHC. The AHC plotted in Fig. 3(c) in the main text are obtained by using the values in the higher probe frequency (6.2-10.3 meV in photon energy) that attain better spatial overlap. By simple calculation with the assumption that the induced AHC is proportional to the pump intensity at each probed position, the AHC at 2 THz will be underestimated by a factor of 0.39. This underestimation can partly cause the discrepancy of AHC between the experiment and the calculation.

This non-uniformity would also explain the incomplete match of the spectral shape between the experiment (Fig. 3(a) and 3(b) in the main text) and the theoretical calculation (Fig. 5(b) and 5(c)). Namely, the slightly smaller AHC in the lower frequency than higher frequency, which does not appear in the theoretically obtained flat spectrum, can be attributed to the spatial non-uniformity which is more prominent in the lower probe frequency.

## APPENDIX G: CARRIER SCATTERING RATE EVALUATED BY THE OPTICAL CONDUCTIVITY SPECTRUM IN THZ FREQUENCY

Figure 8 presents the optical conductivity spectrum of the equilibrium state at room temperature, measured by time-domain THz spectroscopy. The obtained spectrum is well reproduced by the Drude model,  $\sigma(\omega) = \epsilon_0 \omega_p^2 \tau / (1 + i\omega\tau)$  where  $\epsilon_0$ ,  $\omega_p$ ,  $\tau$  are vacuum permittivity, plasma frequency, and carrier scattering time, respectively. Although the scattering rate  $\gamma = \tau^{-1}$  is not accurately determined from the conductivity spectrum within the measured frequency range, the flat spectral shape indicates that the

scattering rate lies much larger than the measured frequency range (2.5 THz at maximum). The fitting by the Drude model provides  $\gamma = 43$  THz corresponding to  $\tau = 23$  fs. Considering the driving frequency by the MIR pump is 75 THz, the electrons in the  $\text{Co}_3\text{Sn}_2\text{S}_2$  film will experience the scattering event within a few cycles of the driving field, which would partially suppress the AHC induced by the CGF.

## APPENDIX H: THE MIR PUMP INDUCED CHANGE IN THE LONGITUDINAL OPTICAL CONDUCTIVITY

Figure 9(a) displays the dynamics of the MIR-pump-induced change in the transmitted probe THz electric field ( $\Delta E_x$ ) divided by its equilibrium value ( $E_x$ ) for the left-hand circular polarization ( $\sigma^-$ , blue) and right-hand circular polarization ( $\sigma^+$ , red). The photon energy and fluence of the MIR pump pulse were set to 0.31 eV and  $2.4 \text{ mJ cm}^{-2}$ , respectively, which are the same as those for the data in Fig. 2B-2F in the main text. The signal shows the maximum value at 0.6 ps, followed by a decaying component with a lifetime of more than 5 ps. The grey line represents the difference between  $\Delta E_x/E_x$  for the  $\sigma^-$  excitation and that for the  $\sigma^+$  excitation, which indicates the absence of the helicity-dependent component in the dynamics of  $\Delta E_x/E_x$ .

The longitudinal optical conductivity spectra,  $\sigma_{xx}(\omega)$ , with various pump fluences are displayed for those under the MIR pulse irradiation ( $t_{pp} = 0$  ps, Fig. 9(b) and 9(c)) and those for the long-lived state ( $t_{pp} = 3$  ps, Fig. 9(d) and 9(e)). The dashed lines present their equilibrium values. The conductivity spectra at  $t_{pp} = 3$  ps show the up to 3 % decrease of  $\text{Re}[\sigma_{xx}]$ . This spectral weight missing in the low frequency range can be caused by a decrease of the carrier density or an increase of the carrier scattering rate. Since it is unlikely that the MIR pump picked off the free carriers at the Fermi surfaces and the created nonequilibrium (not quasi-thermal) state lives for 3 ps, the decrease of  $\text{Re}[\sigma_{xx}]$  is presumably attributed to the increase of the carrier scattering rate. The spectra at  $t_{pp} = 0$  ps shows the similar change as those at  $t_{pp} = 3$  ps.

## APPENDIX I: CONSIDERATION OF THE CONTRIBUTION BY THE INVERSE FARADAY EFFECT

To evaluate the effect of the inverse Faraday effect (IFE) in  $\text{Co}_3\text{Sn}_2\text{S}_2$ , here we consider the CPL-induced Zeeman splitting. The Zeeman splitting term that will be proportional to  $\tau_0 s_z$  does not appear in the CPL-driven massive Dirac state, namely, the sum of  $H_{\text{eff}}(\mathbf{k})$  (eq. (2) in the main text) and  $H_{\text{SO},x} = m\tau_y s_x$ . However, this disappearance depends on the detail of the in-plane SOC, which was added to reproduce the gap at the Dirac points in  $\text{Co}_3\text{Sn}_2\text{S}_2$ . Although we chose the  $k$ -independent term ( $m\tau_y s_x$ ) for

simplicity, various descriptions can also be considered as an origin of the mass gap. Among the possible descriptions, a  $k$ -dependent in-plane SOC term,  $H_{\text{SO},xy}(\mathbf{k}) = -\tilde{m}\tau_0(k_x s_x + k_y s_y)$ , will maximize the Zeeman splitting, the energy of which is estimated as  $-\frac{\tilde{m}^2 E^2}{\Omega^3}$  by simply calculating the effective Floquet Hamiltonian of  $H_{\text{SO},xy}(\mathbf{k})$  under the CPL irradiation. Here,  $\tilde{m} = ma$  where the mass gap energy  $m = 5$  meV and the lattice constant  $a = 5.37$  Å. The calculated Zeeman splitting energy is  $0.11$   $\mu\text{eV}$ , much smaller than the energy splitting induced by the CGF ( $3.1$  meV). Figure 10(a) represents how the band structure is modulated by the effect of CGF and IFE. We here draw a *massless* 3D Dirac state as an initial state for better understanding of the essence. The separation of the emergent WPs is along the  $k_z$  momentum direction in the case of CGF, while that is along the energy direction in the case of IFE. The AHC induced by this Zeeman term with the material parameter set of  $\text{Co}_3\text{Sn}_2\text{S}_2$  is calculated in the same way as that by the CGF, namely, from eq. (A4). We confirmed that the induced AHC by this Zeeman term is negligible compared to that by the CGF, as shown in Fig. 10(b). From the consideration here, we excluded the IFE which is described by the CPL-induced Zeeman splitting as an origin of the observed AHE.

## REFERENCE

- [1] N. P. Armitage, E. J. Mele, and A. Vishwanath, *Weyl and Dirac Semimetals in Three-Dimensional Solids*, Rev. Mod. Phys. **90**, 015001 (2018).
- [2] M. Z. Hasan, G. Chang, I. Belopolski, G. Bian, S.-Y. Xu, and J.-X. Yin, *Weyl, Dirac and High-Fold Chiral Fermions in Topological Quantum Matter*, Nat. Rev. Mater. **6**, 784 (2021).
- [3] J. Hu, S.-Y. Xu, N. Ni, and Z. Mao, *Transport of Topological Semimetals*, Annu. Rev. Mater. Res. **49**, 207 (2019).
- [4] A. A. Burkov, *Topological Semimetals*, Nat. Mater. **15**, 1145 (2016).
- [5] S. Jia, S.-Y. Xu, and M. Z. Hasan, *Weyl Semimetals, Fermi Arcs and Chiral Anomalies*, Nat. Mater. **15**, 1140 (2016).
- [6] B. Yan and C. Felser, *Topological Materials: Weyl Semimetals*, Annu. Rev. Condens. Matter Phys. **8**, 337 (2017).
- [7] N. Nagaosa, T. Morimoto, and Y. Tokura, *Transport, Magnetic and Optical Properties of Weyl Materials*, Nat. Rev. Mater. **5**, 621 (2020).
- [8] A. A. Abrikosov, *Quantum Magnetoresistance of Layered Semimetals*, Phys. Rev. B **60**, 4231 (1999).

- [9] D. T. Son and B. Z. Spivak, *Chiral Anomaly and Classical Negative Magnetoresistance of Weyl Metals*, Phys. Rev. B **88**, 104412 (2013).
- [10] A. A. Burkov, *Chiral Anomaly and Transport in Weyl Metals*, J. Phys. Condens. Matter **27**, 113201 (2015).
- [11] S.-Y. Xu et al., *Observation of Fermi Arc Surface States in a Topological Metal*, Science **347**, 294 (2015).
- [12] A. C. Potter, I. Kimchi, and A. Vishwanath, *Quantum Oscillations from Surface Fermi Arcs in Weyl and Dirac Semimetals*, Nat. Commun. **5**, 5161 (2014).
- [13] K.-Y. Yang, Y.-M. Lu, and Y. Ran, *Quantum Hall Effects in a Weyl Semimetal: Possible Application in Pyrochlore Iridates*, Phys. Rev. B **84**, 075129 (2011).
- [14] F. de Juan, A. G. Grushin, T. Morimoto, and J. E. Moore, *Quantized Circular Photogalvanic Effect in Weyl Semimetals*, Nat. Commun. **8**, 15995 (2017).
- [15] J. Ma, Q. Gu, Y. Liu, J. Lai, P. Yu, X. Zhuo, Z. Liu, J.-H. Chen, J. Feng, and D. Sun, *Nonlinear Photoresponse of Type-II Weyl Semimetals*, Nat. Mater. **18**, 476 (2019).
- [16] D. Rees, K. Manna, B. Lu, T. Morimoto, H. Borrmann, C. Felser, J. E. Moore, D. H. Torchinsky, and J. Orenstein, *Helicity-Dependent Photocurrents in the Chiral Weyl Semimetal RhSi*, Sci. Adv. **6**, eaba0509 (2020).
- [17] G. B. Osterhoudt et al., *Colossal Mid-Infrared Bulk Photovoltaic Effect in a Type-I Weyl Semimetal*, Nat. Mater. **18**, 471 (2019).
- [18] E. J. Sie et al., *An Ultrafast Symmetry Switch in a Weyl Semimetal*, Nature **565**, 61 (2019).
- [19] L. Luo et al., *A Light-Induced Phononic Symmetry Switch and Giant Dissipationless Topological Photocurrent in ZrTe<sub>5</sub>*, Nat. Mater. **20**, 329 (2021).
- [20] N. Sirica et al., *Photocurrent-Driven Transient Symmetry Breaking in the Weyl Semimetal TaAs*, Nat. Mater. **21**, 62 (2022).
- [21] T. Oka and S. Kitamura, *Floquet Engineering of Quantum Materials*, Annu. Rev. Condens. Matter Phys. **10**, 387 (2019).
- [22] M. S. Rudner and N. H. Lindner, *Band Structure Engineering and Non-Equilibrium Dynamics in Floquet Topological Insulators*, Nat. Rev. Phys. **2**, 229 (2020).
- [23] A. Eckardt and E. Anisimovas, *High-Frequency Approximation for Periodically Driven Quantum Systems from a Floquet-Space Perspective*, New J. Phys. **17**, 093039 (2015).



- [24] R. Wang, B. Wang, R. Shen, L. Sheng, and D. Y. Xing, *Floquet Weyl Semimetal Induced by Off-Resonant Light*, EPL Europhys. Lett. **105**, 17004 (2014).
- [25] S. Ebihara, K. Fukushima, and T. Oka, *Chiral Pumping Effect Induced by Rotating Electric Fields*, Phys. Rev. B **93**, 155107 (2016).
- [26] L. Bucciantini, S. Roy, S. Kitamura, and T. Oka, *Emergent Weyl Nodes and Fermi Arcs in a Floquet Weyl Semimetal*, Phys. Rev. B **96**, 041126(R) (2017).
- [27] H. Hübener, M. A. Sentef, U. De Giovannini, A. F. Kemper, and A. Rubio, *Creating Stable Floquet–Weyl Semimetals by Laser-Driving of 3D Dirac Materials*, Nat. Commun. **8**, 13940 (2017).
- [28] C.-K. Chan, Y.-T. Oh, J. H. Han, and P. A. Lee, *Type-II Weyl Cone Transitions in Driven Semimetals*, Phys. Rev. B **94**, 121106(R) (2016).
- [29] T. Sato, K. Segawa, K. Kosaka, S. Souma, K. Nakayama, K. Eto, T. Minami, Y. Ando, and T. Takahashi, *Unexpected Mass Acquisition of Dirac Fermions at the Quantum Phase Transition of a Topological Insulator*, Nat. Phys. **7**, 840 (2011).
- [30] S.-Y. Xu et al., *Topological Phase Transition and Texture Inversion in a Tunable Topological Insulator*, Science **332**, 560 (2011).
- [31] S. Souma, M. Komatsu, M. Nomura, T. Sato, A. Takayama, T. Takahashi, K. Eto, K. Segawa, and Y. Ando, *Spin Polarization of Gapped Dirac Surface States Near the Topological Phase Transition in  $TlBi(S_{1-x}Se_x)_2$* , Phys. Rev. Lett. **109**, 186804 (2012).
- [32] M. Brahlek, N. Bansal, N. Koirala, S.-Y. Xu, M. Neupane, C. Liu, M. Z. Hasan, and S. Oh, *Topological-Metal to Band-Insulator Transition in  $(Bi_{1-x}In_x)_2Se_3$  Thin Films*, Phys. Rev. Lett. **109**, 186403 (2012).
- [33] L. Wu, M. Brahlek, R. Valdés Aguilar, A. V. Stier, C. M. Morris, Y. Lubashevsky, L. S. Bilbro, N. Bansal, S. Oh, and N. P. Armitage, *A Sudden Collapse in the Transport Lifetime across the Topological Phase Transition in  $(Bi_{1-x}In_x)_2Se_3$* , Nat. Phys. **9**, 410 (2013).
- [34] Z. K. Liu et al., *Discovery of a Three-Dimensional Topological Dirac Semimetal,  $Na_3Bi$* , Science **343**, 864 (2014).
- [35] S. Borisenko, Q. Gibson, D. Evtushinsky, V. Zabolotnyy, B. Büchner, and R. J. Cava, *Experimental Realization of a Three-Dimensional Dirac Semimetal*, Phys. Rev. Lett. **113**, 027603 (2014).
- [36] Z. K. Liu et al., *A Stable Three-Dimensional Topological Dirac Semimetal  $Cd_3As_2$* , Nat. Mater. **13**, 677 (2014).
- [37] M. Neupane et al., *Observation of a Three-Dimensional Topological Dirac Semimetal Phase in High-Mobility  $Cd_3As_2$* , Nat. Commun. **5**, 3786 (2014).

- [38] Z. Wang, Y. Sun, X.-Q. Chen, C. Franchini, G. Xu, H. Weng, X. Dai, and Z. Fang, *Dirac Semimetal and Topological Phase Transitions in  $A_3Bi$  ( $A = Na, K, Rb$ )*, Phys. Rev. B **85**, 195320 (2012).
- [39] M. C. Rechtsman, J. M. Zeuner, Y. Plotnik, Y. Lumer, D. Podolsky, F. Dreisow, S. Nolte, M. Segev, and A. Szameit, *Photonic Floquet Topological Insulators*, Nature **496**, 196 (2013).
- [40] G. Jotzu, M. Messer, R. Desbuquois, M. Lebrat, T. Uehlinger, D. Greif, and T. Esslinger, *Experimental Realization of the Topological Haldane Model with Ultracold Fermions*, Nature **515**, 237 (2014).
- [41] J. W. McIver, B. Schulte, F.-U. Stein, T. Matsuyama, G. Jotzu, G. Meier, and A. Cavalleri, *Light-Induced Anomalous Hall Effect in Graphene*, Nat. Phys. **16**, 38 (2020).
- [42] E. Liu et al., *Giant Anomalous Hall Effect in a Ferromagnetic Kagome-Lattice Semimetal*, Nat. Phys. **14**, 1125 (2018).
- [43] Q. Wang, Y. Xu, R. Lou, Z. Liu, M. Li, Y. Huang, D. Shen, H. Weng, S. Wang, and H. Lei, *Large Intrinsic Anomalous Hall Effect in Half-Metallic Ferromagnet  $Co_3Sn_2S_2$  with Magnetic Weyl Fermions*, Nat. Commun. **9**, 3681 (2018).
- [44] A. Ozawa and K. Nomura, *Two-Orbital Effective Model for Magnetic Weyl Semimetal in Kagome-Lattice Shandite*, J. Phys. Soc. Jpn. **88**, 123703 (2019).
- [45] I. Belopolski et al., *Signatures of Weyl Fermion Annihilation in a Correlated Kagome Magnet*, Phys. Rev. Lett. **127**, 256403 (2021).
- [46] D. F. Liu et al., *Topological Phase Transition in a Magnetic Weyl Semimetal*, Phys. Rev. B **104**, 205140 (2021).
- [47] K. Fujiwara, J. Ikeda, J. Shiogai, T. Seki, K. Takanashi, and A. Tsukazaki, *Ferromagnetic  $Co_3Sn_2S_2$  Thin Films Fabricated by Co-Sputtering*, Jpn. J. Appl. Phys. **58**, 050912 (2019).
- [48] Y. Xu et al., *Electronic Correlations and Flattened Band in Magnetic Weyl Semimetal Candidate  $Co_3Sn_2S_2$* , Nat. Commun. **11**, 3985 (2020).
- [49] R. Yang, T. Zhang, L. Zhou, Y. Dai, Z. Liao, H. Weng, and X. Qiu, *Magnetization-Induced Band Shift in Ferromagnetic Weyl Semimetal  $Co_3Sn_2S_2$* , Phys. Rev. Lett. **124**, 077403 (2020).
- [50] Z. Yan and Z. Wang, *Tunable Weyl Points in Periodically Driven Nodal Line Semimetals*, Phys. Rev. Lett. **117**, 087402 (2016).
- [51] T. Oka and H. Aoki, *Photovoltaic Hall Effect in Graphene*, Phys. Rev. B **79**, 081406(R) (2009).

- [52] T. Oka and H. Aoki, *All Optical Measurement Proposed for the Photovoltaic Hall Effect*, J. Phys. Conf. Ser. **334**, 012060 (2011).
- [53] S. A. Sato et al., *Microscopic Theory for the Light-Induced Anomalous Hall Effect in Graphene*, Phys. Rev. B **99**, 214302 (2019).
- [54] S. A. Sato, P. Tang, M. A. Sentef, U. D. Giovannini, H. Hübener, and A. Rubio, *Light-Induced Anomalous Hall Effect in Massless Dirac Fermion Systems and Topological Insulators with Dissipation*, New J. Phys. **21**, 093005 (2019).
- [55] P. Giannozzi et al., *Advanced Capabilities for Materials Modelling with Quantum ESPRESSO*, J. Phys. Condens. Matter **29**, 465901 (2017).
- [56] G. Pizzi et al., *Wannier90 as a Community Code: New Features and Applications*, J. Phys. Condens. Matter **32**, 165902 (2020).
- [57] M. Tanaka et al., *Topological Kagome Magnet  $\text{Co}_3\text{Sn}_2\text{S}_2$  Thin Flakes with High Electron Mobility and Large Anomalous Hall Effect*, Nano Lett. **20**, 7476 (2020).

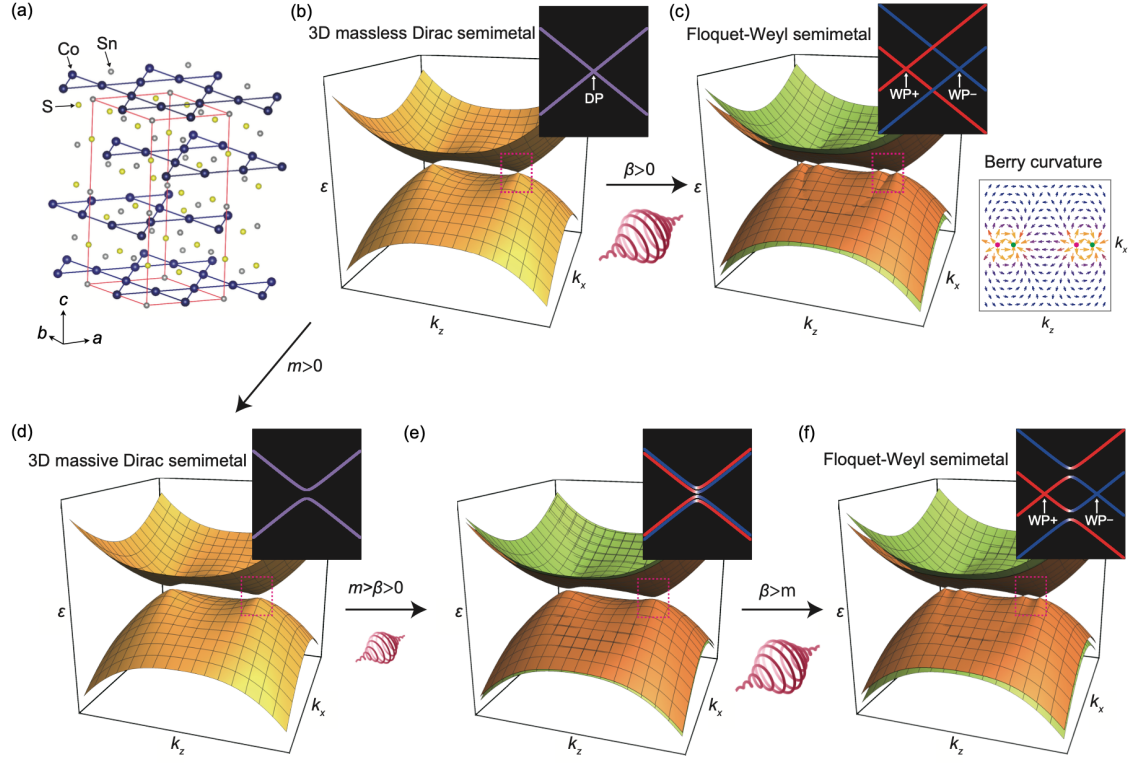


**Figure 1** (a) Crystal structure of  $\text{Co}_3\text{Sn}_2\text{S}_2$  where the cobalt atoms form a kagome lattice. (b) Band structure of massless 3D Dirac state projected onto  $k_y = 0$  plane calculated based on the effective model described in the text. The inset shows the projected energy bands onto  $k_x = 0$  around the Dirac point (DP). (c) Same as (b) for Floquet-Weyl state under CPL irradiation. The Floquet-Weyl points with positive and negative chirality ( $\text{WP}_+$  and  $\text{WP}_-$ ) are indicated in the projected bands. Schematic of Berry curvature distribution is also displayed, where the WPs with chirality plus (minus) are indicated by magenta (green) circles. (d) Same as (b) for massive ( $m > 0$ ) 3D Dirac state. (e) and (f) CPL-induced Floquet band structure with a weak field regime ( $\beta < m$ ) and strong field regime ( $\beta > m$ ), respectively. For insets, the color of the plotted energy bands reflects the spin state; purple indicates the spin-degenerated band, while red, blue, and white indicate the expectation value of the spin  $\langle s_z \rangle = 1, -1$  and  $0$ , respectively.

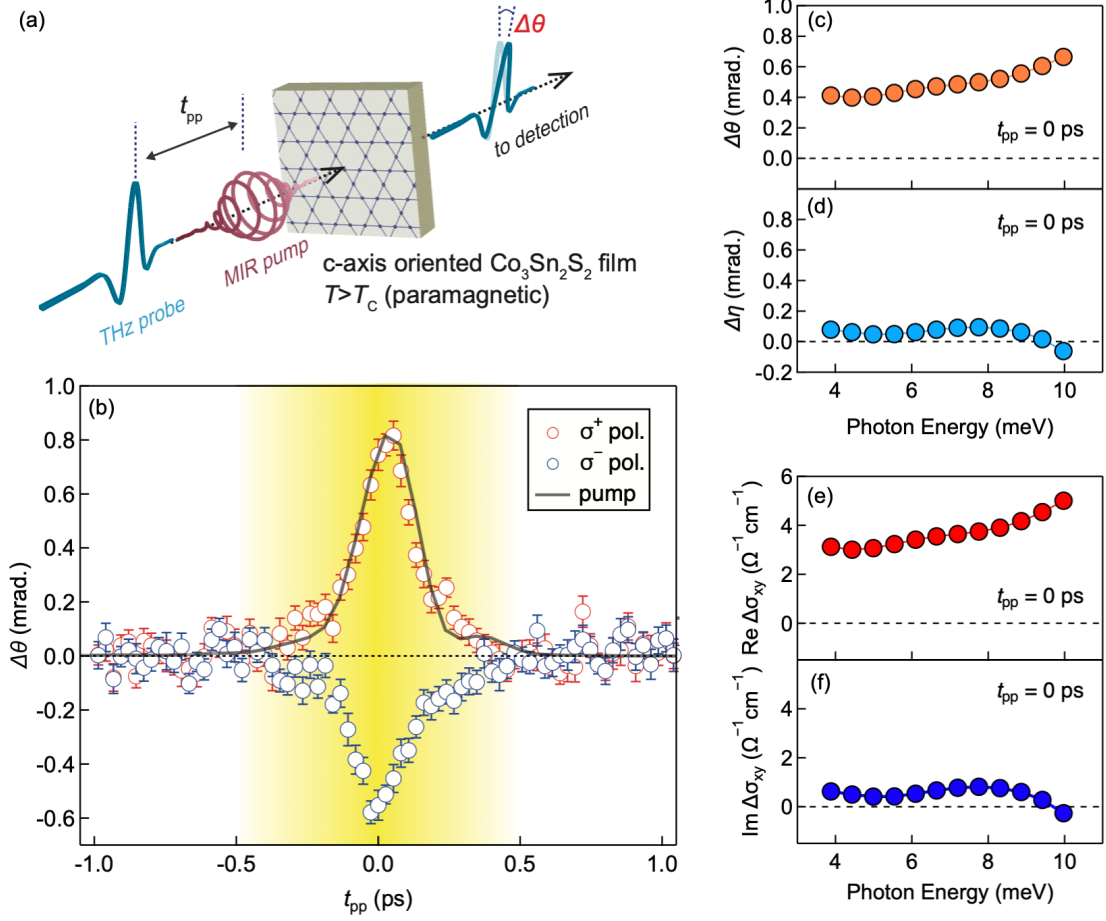


**Figure 2** (a) Schematic of the MIR pump-THz Faraday probe spectroscopy on  $\text{Co}_3\text{Sn}_2\text{S}_2$  film. The MIR pump-induced Faraday rotation of the transmitted THz probe pulse,  $\Delta\theta$ , is measured as a function of pump-probe delay time  $t_{pp}$ . (b) Time evolution of MIR pump-induced Faraday rotation angle  $\Delta\theta$  of the probe THz pulse transmitted through the  $\text{Co}_3\text{Sn}_2\text{S}_2$  film, for left-hand circular polarization ( $\sigma^-$ , blue open circles) and right-hand circular polarization ( $\sigma^+$ , red open circles). The pump fluence was  $2.4 \text{ mJ/cm}^2$ . Grey line indicates the cross-correlation signal of the pump pulse. Error bars indicate the standard errors obtained by multiple measurements. (c) and (d) CPL-induced spectrum of Faraday rotation angle  $\theta$  and ellipticity  $\eta$ , respectively, at  $t_{pp} = 0$  ps. (e) and (f) Real and imaginary part of the CPL-induced AHC, respectively, which are converted from  $\theta$  and  $\eta$ .

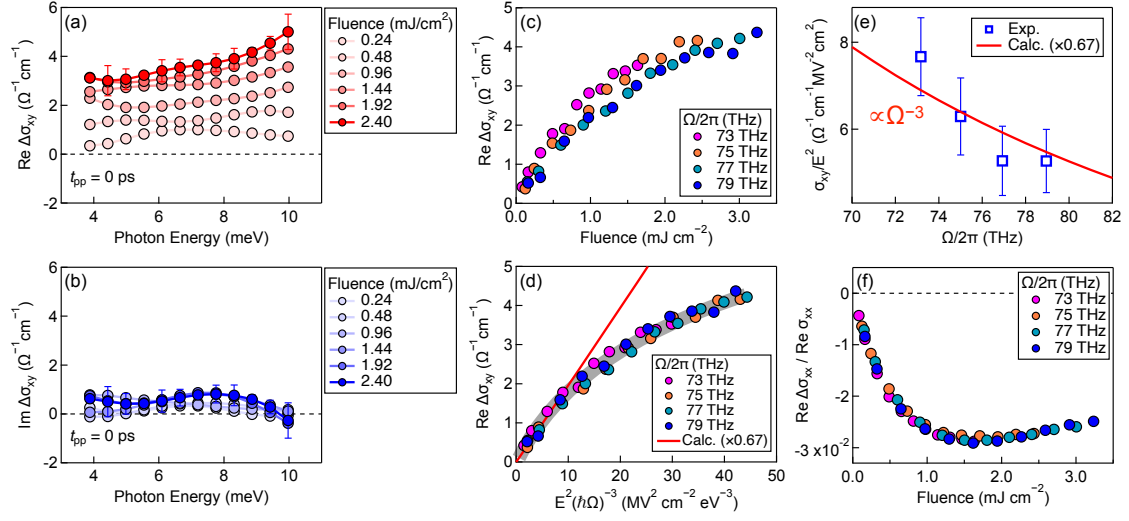


**Figure 3** (a) and (b) Real and imaginary part of the THz AHC spectra, respectively, measured at  $t_{pp} = 0$  with various fluences. Typical values of the standard deviation of multiple measurements are indicated in the data for the highest fluence. (c) Fluence dependence of the CPL-induced THz AHC. Each color indicates the pump frequency. (d) Same data as (c), but plotted as a function of  $E^2(\hbar\Omega)^{-3}$ . Grey line is a guide-to-eye indicating that all the data are aligned in one curve. The calculated value is presented by red line. (e) The frequency dependence of the CPL-induced AHC. Error bars indicate the estimation error of each data. Red line presents the calculation scaled as the same way in (d). (f) Fluence dependence of relative change in longitudinal THz conductivity with various pump frequencies.

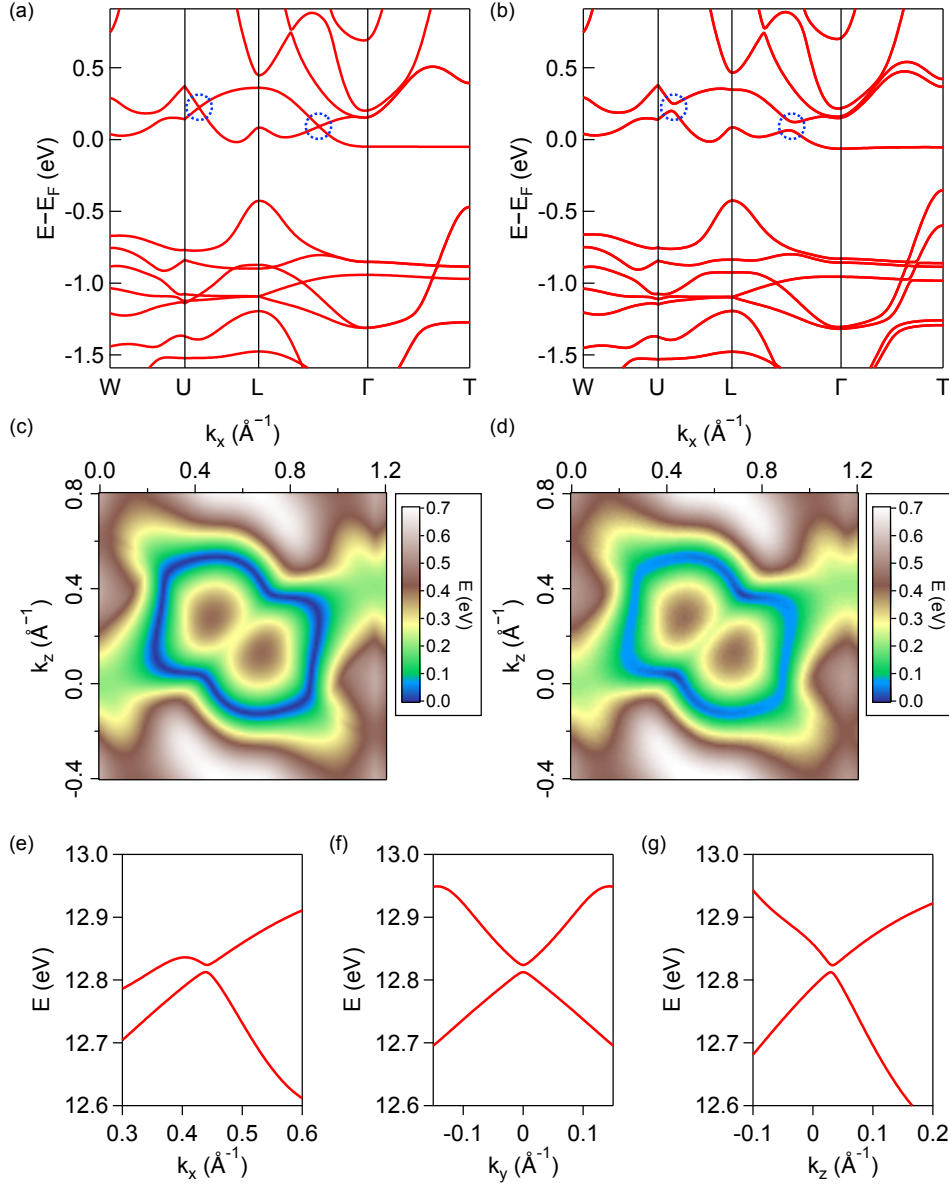


**Figure 4** (a) The band structure of  $\text{Co}_3\text{Sn}_2\text{S}_2$  in the paramagnetic phase along high-symmetry points without SOC. Blue dashed circles denote band crossing. (b) Same as (a) with SOC. Blue dashed circles indicate the gap opening at the band crossing. (c) and (d) Energy separations of the relevant two bands of  $\text{Co}_3\text{Sn}_2\text{S}_2$  in its paramagnetic phase without and with SOC, respectively. (e-g) Band dispersions around the massive DP along  $k_x, k_y, k_z$  directions, respectively.

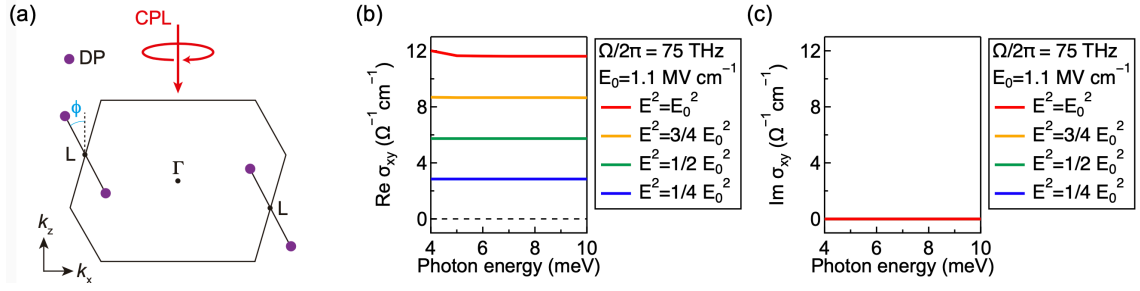


**Figure 5** (a) Illustration of the configuration of the DPs in  $\text{Co}_3\text{Sn}_2\text{S}_2$  and the CPL. Black solid line indicates the first Brillouin zone projected onto the  $k_y = 0$  plane. The CPL propagates along the  $z$ -axis while the separation of the DPs is tilted by angle  $\phi$ . (b) and (c) Calculated spectra of real and imaginary parts of the CPL-induced AHC with various field strengths, respectively.

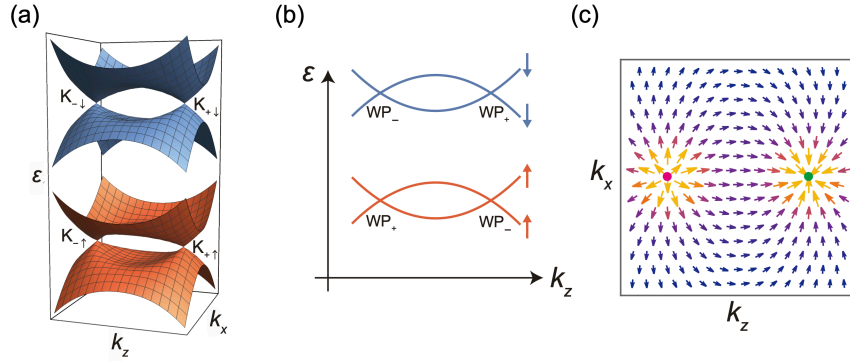


**Figure 6** (a) Schematic band structure of the equilibrium ferromagnetic Weyl phase of  $\text{Co}_3\text{Sn}_2\text{S}_2$  below  $T_C$ , projected onto  $k_y = 0$  plane. The spin-majority (spin-minority) band is drawn by red (blue) planes. The pair of Dirac points at  $K_{\pm}$  in the momentum space is indicated. (b) Projection of the energy band in (A) onto  $k_x = 0$  which includes the two energy lifted pairs of WPs. (c) Schematic of Berry curvature distribution of the spin-majority band of the ferromagnetic Weyl state.



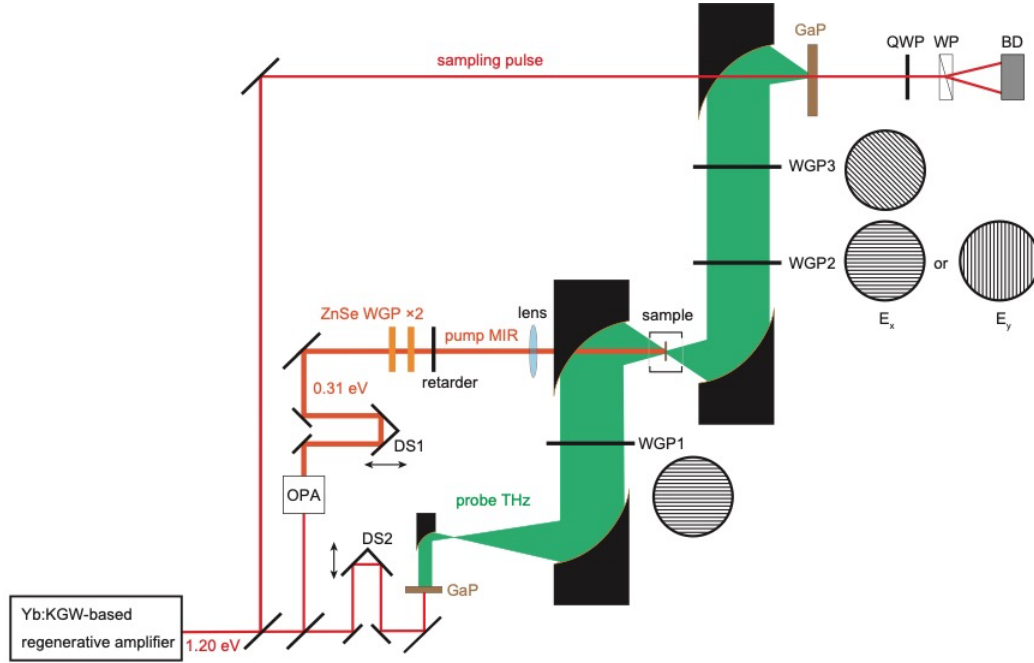


**Figure 7** Experimental setup for the MIR pump-THz Faraday probe measurement. OPA: optical parametric amplifier, DS: delay stage, WGP: wire-grid polarizer, QWP: quarter waveplate, WP: Wollaston prism, BD: balanced photodetector.

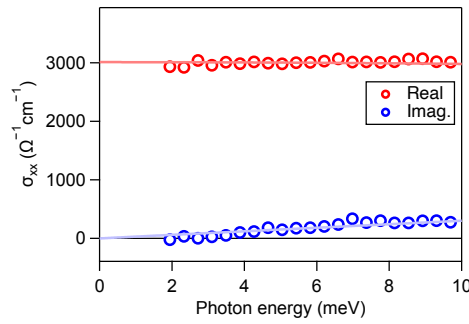


**Figure 8** The real and imaginary parts of the optical conductivity measured by THz time-domain spectroscopy. The line represents the fitting curves by the Drude model.

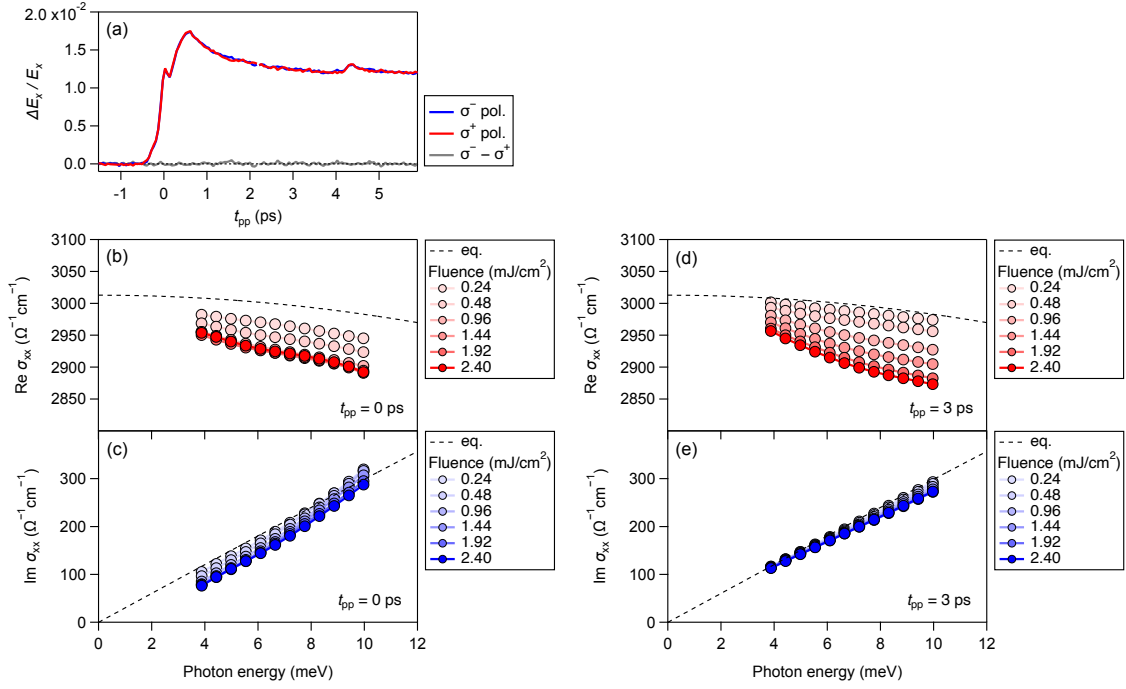


**Figure 9** (a) Time evolution of the transmitted THz electric field  $\Delta E_x$  divided by its equilibrium value  $E_x$ , as a function of the pump-probe delay time  $t_{pp}$ . The data for  $\sigma^-$ ,  $\sigma^+$ ,  $X$  excitation (blue, red, green), and the helicity dependent component (grey) are plotted. The hump at  $t_{pp} \sim 4$  ps is likely attributed to the internal reflection of the pump pulse inside the substrate. (b) and (c) Real and imaginary part of the pump induced change of the longitudinal optical conductivity  $\sigma_{xx}$  at  $t_{pp} = 0$ , with the various pump fluences. The equilibrium values are indicated by dashed lines. (d) and (e) Same as (b) and (c), for  $t_{pp} = 3$  ps.

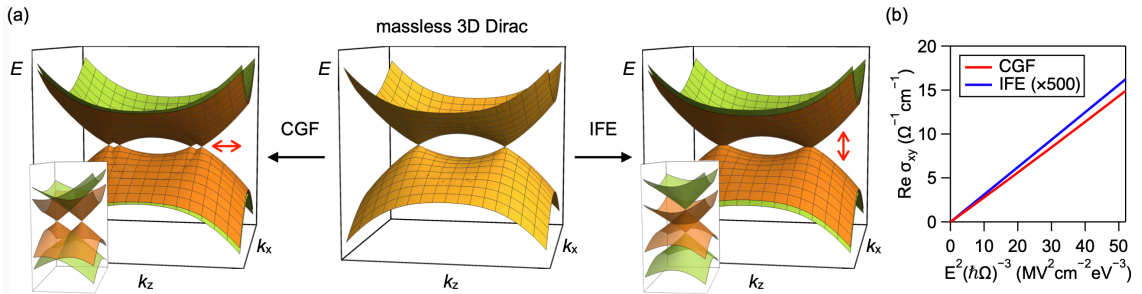


**Figure 10** (a) The band structures showing how the CGF and IFE modulate the massless 3D Dirac state. The insets are enlarged view around the initial DP. (b) AHC in  $\text{Co}_3\text{Sn}_2\text{S}_2$  as a function of  $E^2/(\hbar\Omega)^3$ , induced by the IFE (blue line) and the CGF (red line).